

Water Oxidation Catalyzed by Mononuclear Ruthenium Complexes with a 2,2'-Bipyridine-6,6'-dicarboxylate (bda) Ligand: How Ligand Environment Influences the Catalytic Behavior

Robert Staehle,^{†,‡,§,¶} Lianpeng Tong,^{§,¶} Lei Wang,[§] Lele Duan,[§] Andreas Fischer,[§] Mårten S. G. Ahlquist,^{*,||} Licheng Sun,^{*,§,⊥} and Sven Rau^{*,‡}

[†]Department of Chemistry and Pharmacy, Friedrich-Alexander University of Erlangen-Nuremberg, Schlossplatz 4, 91054 Erlangen, Germany

[‡]Institute for Materials and Catalysis, University of Ulm, Albert-Einstein-Allee 11, 89081 Ulm, Germany

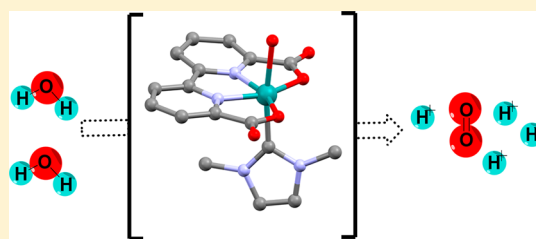
[§]Department of Chemistry, KTH Royal Institute of Technology, Valhallavägen 79, 100 44 Stockholm, Sweden

^{||}Department of Theoretical Chemistry & Biology, School of Biotechnology, KTH Royal Institute of Technology, Valhallavägen 79, 100 44 Stockholm, Sweden

[⊥]State Key Laboratory of Fine Chemicals, Dalian University of Technology, Liaoning, Dalian, China

Supporting Information

ABSTRACT: A new water oxidation catalyst $[\text{Ru}^{\text{III}}(\text{bda})(\text{mmi})(\text{OH}_2)](\text{CF}_3\text{SO}_3)$ (**2**, H_2bda = 2,2'-bipyridine-6,6'-dicarboxylic acid; mmi = 1,3-dimethylimidazolium-2-ylidene) containing an axial N-heterocyclic carbene ligand and one aqua ligand was synthesized and fully characterized. The kinetics of catalytic water oxidation by **2** were measured using stopped-flow technique, and key intermediates in the catalytic cycle were probed by density functional theory calculations. While analogous Ru-bda water oxidation catalysts $[\text{Ru}(\text{bda})\text{L}_2]$ (L = pyridyl ligands) are supposed to catalyze water oxidation through a bimolecular coupling pathway, our study points out that **2**, surprisingly, undergoes a single-site water nucleophilic attack (acid–base) pathway. The diversion of catalytic mechanisms is mainly ascribed to the different ligand environments, from nonaqua ligands to an aqua ligand. Findings in this work provide some critical proof for our previous hypothesis about how alternation of ancillary ligands of water oxidation catalysts influences their catalytic efficiency.



INTRODUCTION

With regard to the rising global demand in energy, seeking alternatives for fossil energy has become one of the greatest challenges nowadays.¹ Solar energy is safe, clean, and sustainable.² A promising way of realizing solar energy utilization is to store the solar energy in the form of a chemical bond via the photosynthetic process, which includes the water oxidation (O_2 evolution) half-reaction ($\text{O}_2 + 4\text{e}^- + 4\text{H}^+ \leftrightarrow 2\text{H}_2\text{O}$, $E^0 = 1.23\text{ V}$ vs NHE at $\text{pH} = 0$) and the proton/ CO_2 reduction half-reaction.^{3,4} In nature, the conversion of solar-to-chemical energy is achieved through a series of sophisticated light-assistant processes, where water oxidation is catalyzed by the oxygen-evolving complex (OEC) of PSII.^{5,6} Mimicking or even surpassing the functional activity of the OEC is a critical subject in the envisaged construction of an artificial photosynthetic system. So far, molecular water oxidation catalysts (WOCs) based on numerous transition metals, such as ruthenium,^{7–10} iridium,^{11,12} manganese,^{13,14} cobalt,^{15,16} and iron^{17,18} have been studied and reported. Among these models of homogeneous WOCs, binuclear and mononuclear ruthenium complexes are widely discussed. Examination upon these ruthenium WOCs, from both the mechanism and activity

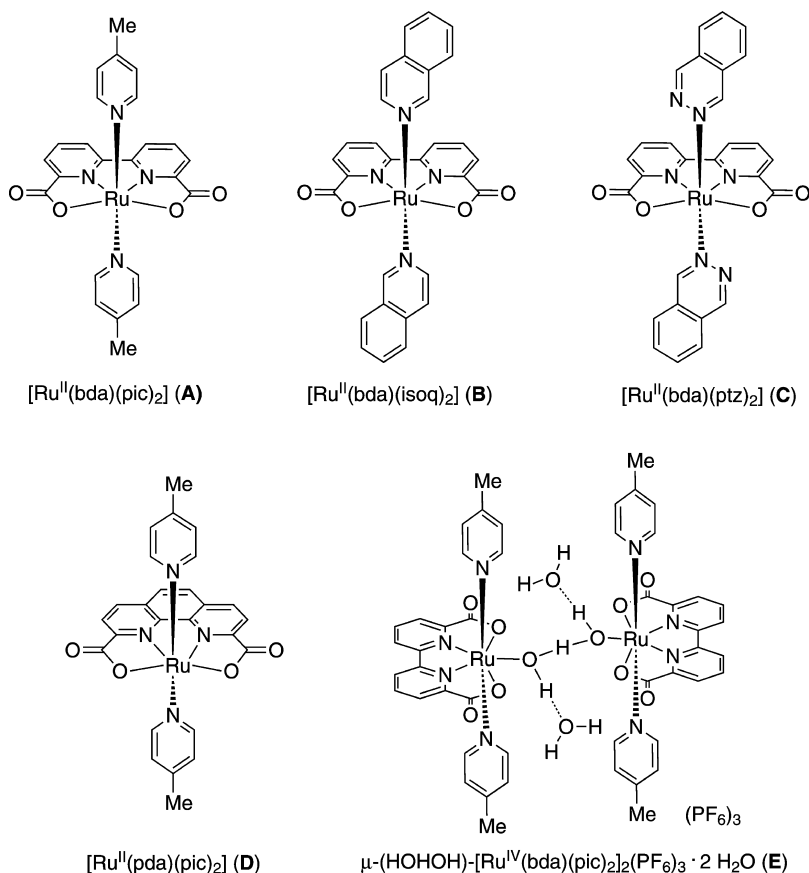
aspects, dramatically inspired the development of other transition-metal-based WOCs afterward.

Recently, Sun and co-workers developed a family of mononuclear ruthenium complexes which show very high efficiency toward catalytic water oxidation.¹⁹ All the ruthenium catalysts share the same octahedral coordination geometry, which includes an equatorial anionic tetradentate bda (H_2bda = 2,2'-bipyridine-6,6'-dicarboxylic acid) ligand, and two axial monodentate N-heterocyclic ligands, for example, 4-picoline (pic), isoquinoline (isoq), or phthalazine (ptz) (Scheme 1, compounds A–C). This type of Ru complex is able to catalyze water oxidation with an impressive efficiency (tens to hundreds of turnovers per second) which is even comparable to that of the OEC.²⁰ On the basis of the isolation of a seven-coordinate ruthenium intermediate (compound E in Scheme 1) and the kinetics of the catalytic water oxidation reaction by A, the family of Ru-bda complexes is supposed to catalyze water oxidation through a bimolecular coupling pathway.^{20,21} In this

Received: July 3, 2013

Published: January 14, 2014

Scheme 1. Structures of Ruthenium WOCs Prepared by the Sun Group (A–D) and the Isolated Seven-Coordinate μ -(HOHOH)-[Ru^{IV}(bda)(pic)₂]₂(PF₆)₃·2H₂O Intermediate (E)



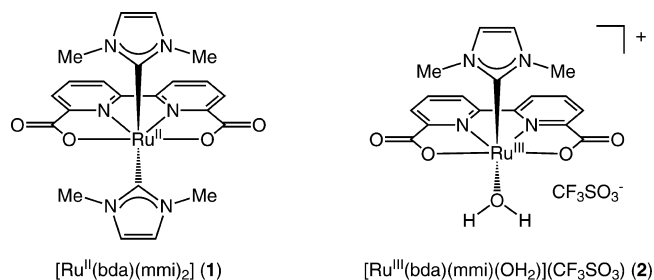
scenario, the O–O bond is formed by coupling of two pentavalent Ru-oxo species.

It has been found that the catalytic activity of Ru-bda complexes is quite sensitive to their ligand environments.^{22,23} By replacing the axial ligand from 4-picoline (in the case of A) to isoquinoline (in the case of B), for instance, the catalytic efficiency of the candidate is drastically promoted from a turnover frequency (TOF) of 32 s^{−1} (for A) to a TOF of 303 s^{−1} (for B).²⁰ Minor modification of the equatorial ligand from flexible bda (of A) to preorganized pda (of D, H₂pda = 1,10-phenanthroline-2,9-dicarboxylic acid) leads to the change of the bimolecular coupling pathway (for A) to a single-site water nucleophilic attack pathway (for D).^{7,8,24–26}

Moreover, it has been observed that stronger Ru–N(axial ligand) bonds of Ru-bda complexes result in greater longevity of their catalytic activity.²⁷ For example, the Ru–N-(phthalazine) bond of C is more resistant to ligand dissociation than the Ru–N(4-picoline) bond of A. In the catalytic O₂-evolving experiments, as a consequence, C preserved its catalytic activity for more than an hour, while A became totally inactive after several minutes of reaction. On the basis of these observations, we proposed that this family of Ru-bda WOCs undergo water/monodentate nitrogen ligand (their axial ligands) exchange during O₂-evolving reaction, and the resulting aqua Ru complexes cannot maintain the high catalytic efficiency for water oxidation.²⁷ Apparently aqua and monodentate nitrogen ligands have a very different electronic and steric effect over the Ru-bda complexes. However, no Ru-bda intermediate containing an axial aqua ligand has been isolated in our previous work. As the influence of the axial

ligand on the catalytic activity has been proven, introducing new structures at these positions is very interesting. N-Heterocyclic carbenes (NHC) are potential candidates for this task since their σ -donor and π -acceptor properties are easily tunable. Herein, we would like to report the synthesis, properties, and catalytic activity of the first Ru-bda complex [Ru^{II}(bda)(mmi)₂] (1, mmi = 1,3-dimethylimidazolium-2-ylidene, Scheme 2; left) containing NHC ligands. This provides

Scheme 2. Structures of [Ru^{II}(bda)(mmi)₂] (1) and [Ru^{III}(bda)(mmi)(OH₂)](CF₃SO₃) (2)



us with an opportunity to study the effect of NHC-ligands on the properties of the Ru-bda fragment and what happens after one axial ligand of Ru-bda WOCs is substituted by a water molecule. Furthermore, comparing [Ru^{III}(bda)(mmi)(OH₂)](CF₃SO₃) 2 (Scheme 2; right) with the previous examples of Ru-bda WOCs (A–C) elucidates the role of ancillary ligands in the context of catalytic O₂ evolution by molecular ruthenium complexes.

EXPERIMENTAL SECTION

General Procedures. ^1H and ^{13}C NMR spectra were recorded with a Bruker Advance 500 spectrometer. The chemical shifts, δ , are given in parts per million relative to TMS ($\delta = 0$), referred internally to the residual proton chemical shift in the deuterated solvent. Solvent peaks were omitted for clarity. The absorbance spectrum was recorded with a Jasco V-670 spectrophotometer, using a quartz glass cuvette of $10 \times 10 \text{ mm}^2$. The ESI-MS measurements were performed with a Finnigan LCQ Advantage MAX. High-resolution mass spectrometry (HRMS) was performed using a Fourier transform ion cyclotron resonance (FT-ICR) mass spectrometer solariX (Bruker Daltonik GmbH, Bremen, Germany) equipped with a 7.0 T superconducting magnet and interfaced to an Apollo II Dual ESI/MALDI source. Electrochemical data were obtained from cyclic voltammetry or differential pulse voltammetry (DPV) using an Autolab potentiostat in a conventional single-compartment three-electrode cell including pyrolytic graphite electrode (basal plane) as the working electrode, platinum wire as the auxiliary electrode, and saturated calomel electrode (SCE) as the reference electrode. $[\text{Ru}^{\text{II}}(\text{bpy})_3]^{2+}$ ($E_{1/2} = 1.26 \text{ V}$ vs NHE) was used as an external reference, and all potentials reported here are referred to the normal hydrogen electrode (NHE). Two phosphate buffered solutions of $[\text{Ru}^{\text{III}}(\text{bda})(\text{mmi})(\text{OH}_2)](\text{CF}_3\text{SO}_3)$ (0.5 mM, pH = 2.4 and 6.3, respectively) were employed in the electrochemical measurements. Their pH value was adjusted by adding small amounts of aqueous HClO_4 or NaOH solution and determined by a pH-meter (Metrohm 781). The kinetic measurements were performed by a stopped-flow instrument Bio-Logic SFM300 coupled with a xenon light source and a fast JM TIDAS UV-vis diode array spectrophotometer. Spectral changes were detected in the wavelength range 300–500 nm. The temperature during measurements was maintained by a thermostatted bath (Polystate 36, Fisher Scientific). The data used for the interpretation was collected after the system was stabilized and reached steady state. Diffraction data for the crystal structure determinations were collected on a Bruker-Nonius KappaCCD diffractometer (Mo $K\alpha$ radiation, $T = 299 \text{ K}$). The perchlorate ion in $[\text{Ru}^{\text{III}}(\text{bda})(\text{mmi})(\text{OH}_2)](\text{ClO}_4)$ (**3**) was refined applying a disordered model. Some restraints were applied in order to achieve satisfactory bond lengths and angles in the water molecules in the triflate structure. *cis*- $[\text{Ru}^{\text{II}}(\text{dmso})_4\text{Cl}_2]$ was synthesized according to the literature procedure.²⁸ The 70% HNO_3 (99.999% purity) and $(\text{NH}_4)_2[\text{Ce}^{\text{IV}}(\text{NO}_3)_6]$ (99.99% purity) were purchased from Sigma-Aldrich and used without further purification. Water used in both syntheses and measurements was deionized by Milli-Q technique. All other chemicals were used as supplied without extra treatment.

Synthesis of $[\text{Ru}^{\text{II}}(\text{bda})(\text{mmi})_2]$ (1**).** Under nitrogen atmosphere, 200 mg (0.4 mmol, 1 equiv) of $[\text{Ru}^{\text{II}}(\text{dmso})_4\text{Cl}_2]$ and 101 mg of 2,2'-bipyridine-6,6'-dicarboxylic acid (0.4 mmol, 1 equiv) were suspended in 100 mL of CH_2Cl_2 . The suspension was stirred under reflux for 30 min. Then, 0.2 mL of NEt_3 (1.7 mmol, 4 equiv, $\rho = 0.73 \text{ g/mL}$) was added, and the solution was refluxed for another 4 h. During this reaction time, the color of solution changed from light yellow to dark red. Subsequently 370 mg (1.7 mmol, 4 equiv) of 1,3-dimethylimidazolium iodide and 191 mg (0.8 mmol, 2 equiv) of silver(I) oxide were added, and the solution was refluxed for 20 h. After the solution cooled to room temperature, 200 mg of K_2CO_3 and 10 mL of CH_3OH were added, and the suspension was stirred for 30 min for work up. The solids in the mixture were filtered off, and the solvents were removed under reduced pressure. Purification was performed via column chromatography over silica gel with gradient elution $\text{CH}_2\text{Cl}_2 \rightarrow \text{CH}_2\text{Cl}_2/\text{CH}_3\text{OH}$ (10:1/v/v), yielding the desired product, 41 mg (19%). ^1H NMR (CD_3OD , $\text{Na}_2\text{S}_2\text{O}_3 \cdot 5\text{H}_2\text{O}$; 500 MHz): δ (ppm) = 8.45 (dd; 2H; $^3J = 8.1 \text{ Hz}$, $^4J = 0.9 \text{ Hz}$), 7.99 (dd; 2H; $^3J = 7.6 \text{ Hz}$, $^4J = 0.9 \text{ Hz}$), 7.82 (dd; 2H; $^3J = 7.9 \text{ Hz}$, $^4J = 7.9 \text{ Hz}$), 6.79 (s, 4H), 3.24 (s, 12 H). MS (ESI, H_2O) Calcd: $m/z = 536.1$ ($[\text{M}]^+$). Found: $m/z = 536.0$. Calcd: $m/z = 559.1$ ($[\text{M} + \text{Na}]^+$). Found: $m/z = 558.9$.

Synthesis of $[\text{Ru}^{\text{III}}(\text{bda})(\text{mmi})(\text{OH}_2)](\text{CF}_3\text{SO}_3)$ (2**).** A 31 mg portion of $[\text{Ru}^{\text{II}}(\text{bda})(\text{mmi})_2]$ (**1**) was dissolved in 10 mL of aqueous $\text{CF}_3\text{SO}_3\text{H}$ (pH = 1)/ $\text{CF}_3\text{CH}_2\text{OH}$ (2:1/v/v) solution. Upon exposure

to air for a few minutes, the color of the solution changed from purple to bright orange, indicating the oxidation of **1** to its trivalent state. By slowly evaporating of the solvent in a small open-end beaker for several days, crystals of **2** were obtained. The crystals were filtered off and washed with a small amount of cold water. Finally the crystals were dried in air (28 mg, yield = 75%). ^1H NMR of the reduced species of **2** (D_2O , $\text{Na}_2\text{S}_2\text{O}_3 \cdot 5\text{H}_2\text{O}$; 500 MHz): δ (ppm) = 8.31 (d; 2H; $^3J = 8.0$), 7.98 (d; 2H; $^3J = 7.5$), 7.77 (dd; 2H; $^3J = 7.9$, $^4J = 7.9$), 6.78 (s; 2H), 3.14 (s; 6H). MS (HR-ESI; aqueous $\text{CF}_3\text{SO}_3\text{H}$ solution, pH = 2) Calcd: $m/z = 440.01$ ($[\text{M} - \text{CF}_3\text{SO}_3 - \text{H}_2\text{O}]^+$). Found: $m/z = 440.00$. Calcd: $m/z = 458.02$ ($[\text{M} - \text{CF}_3\text{SO}_3]^+$). Found: $m/z = 458.01$. Calcd: $m/z = 590.97$ ($[\text{M} - \text{H}_2\text{O} + 2\text{H}]^+$). Found: $m/z = 590.97$. The obtained crystals were suitable for X-ray diffraction crystallography. Crystal data: $[\text{C}_{17}\text{H}_{16}\text{N}_4\text{O}_3\text{Ru}](\text{CF}_3\text{SO}_3) \cdot 2\text{H}_2\text{O}$, $M = 642.5 \text{ g mol}^{-1}$, dark red block, $0.11 \times 0.21 \times 0.44 \text{ mm}^3$, triclinic, $P\bar{1}$, $a = 786.61(15) \text{ pm}$, $b = 1181.20(13) \text{ pm}$, $c = 1303.10(14) \text{ pm}$, $\alpha = 87.294(12)^\circ$, $\beta = 77.555(9)^\circ$, $\gamma = 86.783(16)^\circ$, $V = 1179.7(3) \times 10^6 \text{ pm}^3$, $T = 299 \text{ K}$, $Z = 2$, $\rho_{\text{calcd}} = 1.803 \text{ Mg m}^{-3}$, $\mu(\text{Mo } K\alpha) = 0.84 \text{ mm}^{-1}$, absorption correction multiscan, $F(000) = 646$, 24 314 reflections, $4.6^\circ < \theta < 27.5^\circ$, 5388 independent reflections, 4406 reflections with $I > 2\sigma(I)$, 348 L.S. parameters, $R1 = 0.031$, $wR2 = 0.067$, $\text{GOF} = 1.02$, Fourier map peak/hole $0.46/-0.42 \text{ e/\AA}^3$. CCDC 941974 contains the supplementary crystallographic data for this Article. These data can be obtained free of charge from The Cambridge Crystallographic Data Centre via www.ccdc.cam.ac.uk/data_request/cif.

Synthesis of $[\text{Ru}^{\text{III}}(\text{bda})(\text{mmi})(\text{OH}_2)](\text{ClO}_4)$ (3**).** $[\text{Ru}^{\text{III}}(\text{bda})(\text{mmi})(\text{OH}_2)](\text{ClO}_4)$ was obtained by a method similar to the preparation of **2**. Accordingly, 5 mg of $[\text{Ru}^{\text{II}}(\text{bda})(\text{mmi})_2]$ (**1**) was dissolved in $\sim 3 \text{ mL}$ aqueous HClO_4 (pH = 1)/ $\text{CF}_3\text{CH}_2\text{OH}$ (2:1/v/v) solution. The color of the solution also changed from purple to bright orange within several minutes, indicating the oxidation of the complex **1**. By slow evaporation of the solvent in a small open-end beaker for several days, suitable crystals for X-ray diffraction crystallography were obtained. Crystal data: $[\text{C}_{17}\text{H}_{18}\text{N}_4\text{O}_3\text{Ru}]^+[\text{ClO}_4]^- \cdot \text{H}_2\text{O}$, $M = 574.9 \text{ g mol}^{-1}$, dark red block, $0.3 \times 0.3 \times 0.3 \text{ mm}^3$, monoclinic, $P2_1/n$, $a = 1090.19(6) \text{ pm}$, $b = 1018.3(1) \text{ pm}$, $c = 1891.79(13) \text{ pm}$, $\beta = 99.319(6)^\circ$, $V = 2072.5(3) \times 10^6 \text{ pm}^3$, $T = 299 \text{ K}$, $Z = 4$, $\rho_{\text{calcd}} = 1.842 \text{ Mg m}^{-3}$, $\mu(\text{Mo } K\alpha) = 0.95 \text{ mm}^{-1}$, absorption correction multiscan, $F(000) = 1156$, 23 726 reflections, $4.5^\circ < \theta < 27.5^\circ$, 4725 independent reflections, 3805 reflections with $I > 2\sigma(I)$, 336 L.S. parameters, $R1 = 0.028$, $wR2 = 0.070$, $\text{GOF} = 1.07$, Fourier map peak/hole $0.39/-0.59 \text{ e/\AA}^3$. CCDC 941975 contains the supplementary crystallographic data for this Article. These data can be obtained free of charge from The Cambridge Crystallographic Data Centre via www.ccdc.cam.ac.uk/data_request/cif. No further characterization was performed.

O_2 -Evolving Measurements. A typical run of Ce^{IV} -driven water oxidation was conducted in a flask equipped with 3 mL of aqueous $\text{Ce}^{\text{IV}}/\text{HNO}_3$ solution (initial pH = 1.0; the concentration of $(\text{NH}_4)_2[\text{Ce}^{\text{IV}}(\text{NO}_3)_6]$ is 167 mM). A certain amount of catalyst **2** (1.0 mM in water) was injected into the homogeneous $\text{Ce}^{\text{IV}}/\text{HNO}_3$ solution through a septum cap. The amount of evolved dioxygen was monitored by a pressure transducer (Omega PX138-030A5 V) driven at 8.00 V (power supply TTi-PL601). The data were collected by a data acquisition module (Omega OMB-DAQ-2416). At the end-point of each trial, the gas sample was calibrated by a gas chromatographic measurement (GC-2014 Shimadzu, the oxygen in air was detracted) which is equipped with a thermal conductive detector and a 5 Å molecular sieve column (12 mm/320 mm/10m), and uses He as carrier gas. The TON was reported as the average of three independent measurements.

Theoretical Studies. All density functional theory (DFT) calculations were carried out with the *Jaguar* 7.6 program package by Schrödinger LLC. For geometry optimizations, solvation energy, and frequency calculations, Becke's three-parameter hybrid functional and the LYP correlation functional (B3LYP)^{29,30} were used with the LACVP** core potential and basis set. Meanwhile single-point energy corrections were performed with the M06 functional³¹ using the LACVP3P**++ basis set, which, as suggested by Martin,³² was augmented with two f-polarization functions on the ruthenium metal

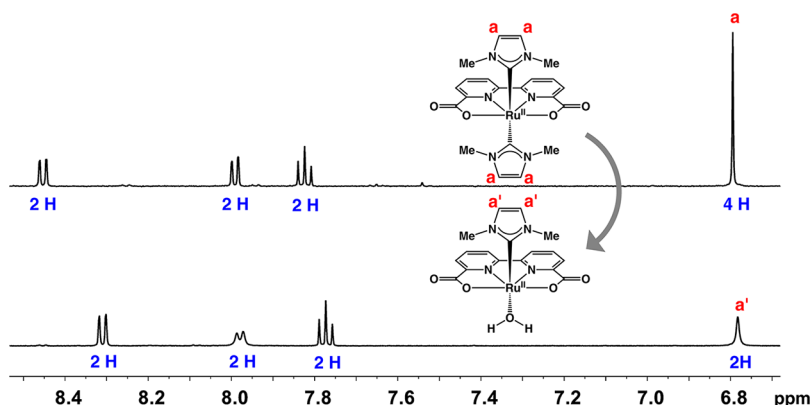
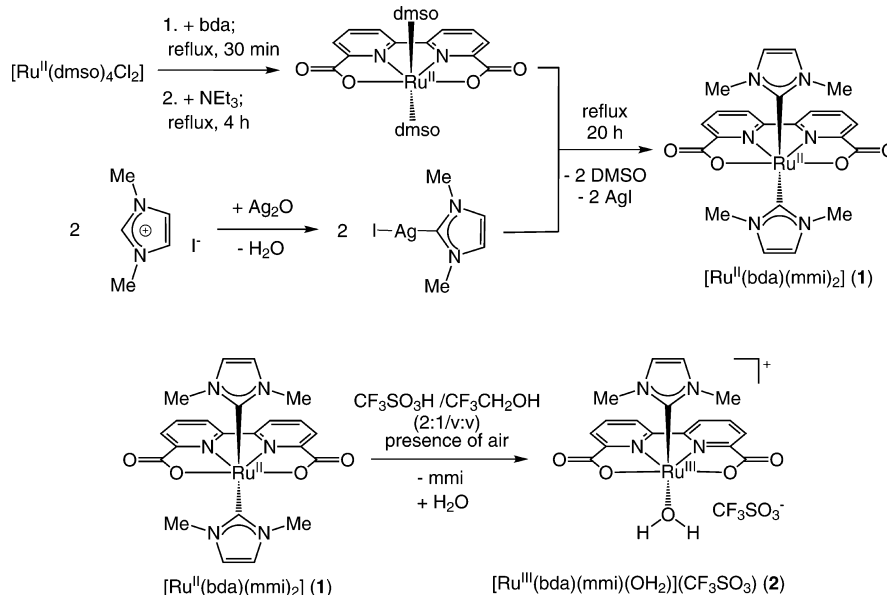
Scheme 3. Synthesis of $[\text{Ru}^{\text{II}}(\text{bda})(\text{mmi})_2]$ (**1**, Top) and $[\text{Ru}^{\text{III}}(\text{bda})(\text{mmi})(\text{OH}_2)](\text{CF}_3\text{SO}_3)$ (**2**, Bottom)

Figure 1. Aromatic region of the ^1H NMR spectrum of **1** in CD_3OD (top) and **2** in D_2O (bottom) reduced by $\text{Na}_2\text{S}_2\text{O}_3$. The blue marks indicate the respective integral of peaks.

center. Frequency calculations were performed on the optimized geometries to verify that the geometries correspond to minima or first-order saddle points (transition states) on the potential energy surface. The Gibbs free energies were defined according to the following equation: $G = E(\text{M06/LACV3P}^{**++2f} \text{ on Ru}) + G_{\text{sol}} + \text{ZPE} + H_{298} - TS_{298} + 1.9$ [concentration correction to the free energy of solvation from 1 M(g) \rightarrow 1 M(aq) to 1 atm(g) \rightarrow 1 M(aq)]. The solvation model applied was the Poisson–Boltzmann reactive field implemented in *Jaguar* 7.6.³³ Experimental value of -270.3 kcal/mol was used for the free energy of solvating proton (at $\text{pH} = 0$).³⁴

RESULTS AND DISCUSSION

Synthesis, Characterization, and Structures. The synthesis of **1** was achieved in a sequential two-step one-pot reaction in boiling dichloromethane under inert conditions (Scheme 3, top). First $[\text{Ru}^{\text{II}}(\text{dmsO})_4\text{Cl}_2]$ and H_2bda were stirred under reflux to ensure that the ruthenium complex is fully dissolved and a precoordination occurs between Ru and bda. Triethylamine was present in the reaction solution in order to deprotonate the H_2bda yielding the bda^{2-} ligand. The carbene precursor was generated *in situ* by adding 1,3-dimethylimidazolium iodide and silver(I) oxide into the reaction system at the same time.³⁵ Extra attention was paid

during the operation to avoid decomposition of the carbene precursor and oxidation of the bivalent ruthenium complexes which are sensitive to air (*vide infra*). The ^1H NMR spectrum of **1** agrees with a C_{2v} structure of the complex under NMR experimental conditions. A group of ABC pattern peaks were observed in the region of 7.6–8.5 ppm (Figure 1), which correspond to the protons of the equatorial bda ligand of **1**. The two axial mmi ligands are identical according to ^1H NMR data. A clear singlet at 6.8 ppm is assigned to the four protons at both mmi rings. The formation of complex **1** was further confirmed by mass spectrometry ($m/z = 536.0$ ($[\text{M}]^+$)).

Complex **1** is expected to adopt the same coordination sphere as other Ru-bda complexes A–C. Compared to the monodentate N-heterocyclic axial ligands in A–C, however, the carbene ligand (mmi) in **1** is a better σ -donating group (less electronegative). We observed that complex **1** is not able to stay intact in the presence of air (oxygen and moisture). After standing for several hours under aerobic conditions, the color of the aqueous solution of **1** changed from purple to orange. This transition of **1** is ascribed to the oxidation of the complex or ligand dissociation from its metal center. The resulting ruthenium species (denoted as complex salt **2**), from oxidation or ligand exchange, is much more stable and can sustain in

acidic aqueous solution for several days. We figured out that this ruthenium species (**2**) might be an important catalyst for water oxidation and a more suitable candidate in the kinetic studies afterward. Thereby, a method was developed explicitly to isolate and identify this intermediate (**2**) that was derived from **1** in acidic aqueous medium.

The detailed procedure of synthesis of **2** has been described in the Experimental Section. Briefly, **2** was isolated as orange crystals by slowly evaporating the organic solvent of an aqueous $\text{CF}_3\text{SO}_3\text{H}$ ($\text{pH} = 1$)/ $\text{CF}_3\text{CH}_2\text{OH}$ (2:1/v:v) solution of **1** (Scheme 3, bottom). The ^1H NMR spectrum of **2** does not reveal any recognizable proton signals. Thus, we proposed that **2** is not a bivalent ruthenium complex and displays paramagnetic property. After the reductive agent $\text{Na}_2\text{S}_2\text{O}_3$ was added in the solution of **2**, the ^1H NMR spectrum of a reduced sample showed a group of ABC type resonance signals (doublets, doublets, and triplets in the region 7.7–8.4 ppm) which are very similar to the signals from the bda ligand shown in the downfield of the ^1H NMR spectrum of **1** (Figure 1). Meanwhile, a singlet peak (6.8 ppm) was observed and assigned to the protons at the ring of the imidazole carbene ligand. Nevertheless, the integral of the singlet peak is 2H, different from the 4H integral in the case of the ^1H NMR spectrum of **1** (Figure 1). Furthermore, the integrals of the methyl groups of the imidazole ring show the same trend. On the basis of these results from ^1H NMR experiments, we proposed that **1** was oxidized to the trivalent state and one of its axial carbene ligands was replaced by a water molecule during the $\mathbf{1} \rightarrow \mathbf{2}$ conversion. Therefore, the resulting complex salt **2** is assigned as $[\text{Ru}^{\text{III}}(\text{bda})(\text{mmi})(\text{OH}_2)](\text{CF}_3\text{SO}_3)$. Signals corresponding to the aqua ligand of **2** could not be identified due to proton exchange within the deuterated water medium. The structure of **2** was further confirmed by mass spectrometry ($m/z = 458.01$ ($[\text{M} - \text{CF}_3\text{SO}_3]^+$)). Final proof of the proposed structure of **2** was obtained from X-ray crystallography (*vide infra*). There are primarily two factors contributing to the labile $\text{Ru}-\text{C}(\text{mmi})$ bonds of **1**. One is the steric repulsion between methyl group of mmi and bda, which pushes the mmi ligand away from the Ru center. The other is the *trans* effect of these two mmi ligands, which destabilizes the $\text{Ru}-\text{C}(\text{mmi})$ coordination bond.³⁶ Ready cleavage of the $\text{Ru}-\text{C}(\text{carbene})$ bond has also been investigated for other ruthenium catalysts in metathesis reactions.³⁷ UV-vis spectrum of **2** shows strong absorbance due to $\pi \rightarrow \pi^*$ transitions at 260 and 290 nm and absorbance due to CT transitions at 350 and 420 nm (Supporting Information Figure S1).

The obtained crystals of **2**, by following the synthetic procedure described above, were suitable for single-crystal X-ray diffraction crystallography (Figure 2). Besides complex salt **2**, we also prepared and isolated the trivalent $[\text{Ru}^{\text{III}}(\text{bda})(\text{mmi})(\text{OH}_2)]^+$ complex with ClO_4^- as counterion, so as to have a closer look at the counterion effect over the structure of the Ru^{III} complex. We marked $[\text{Ru}^{\text{III}}(\text{bda})(\text{mmi})(\text{OH}_2)](\text{ClO}_4)$ as complex salt **3** in order to distinguish it from complex salt **2** with CF_3SO_3^- counterions. The synthetic method of **3** is very similar to that of **2**, but an aqueous HClO_4 solution ($\text{pH} = 1$) was applied instead of an aqueous $\text{CF}_3\text{SO}_3\text{H}$ solution ($\text{pH} = 1$). Obtained crystals of $[\text{Ru}^{\text{III}}(\text{bda})(\text{mmi})(\text{OH}_2)](\text{ClO}_4)$ (**3**) were also suitable for single-crystal X-ray diffraction crystallography (Supporting Information Figure S2). In the case of either **2** or **3**, the cationic ruthenium moiety possesses distorted octahedral coordination geometry. The ruthenium center is surrounded by a nearly planar bda ligand in

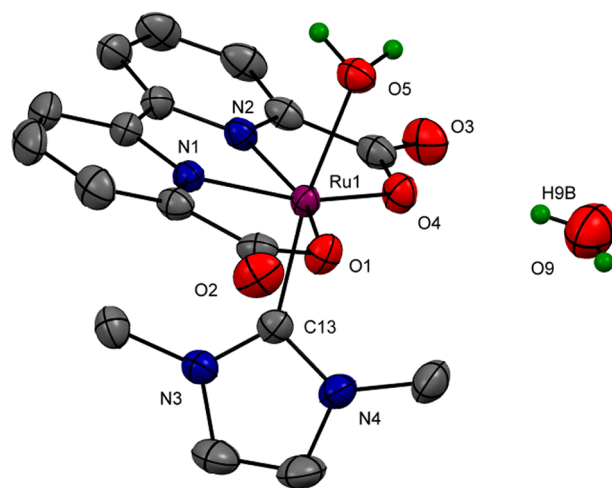


Figure 2. X-ray crystal structure of $[\text{Ru}^{\text{III}}(\text{bda})(\text{mmi})(\text{OH}_2)](\text{CF}_3\text{SO}_3) \cdot 2\text{H}_2\text{O}$ (**2**, ellipsoids at 50% probability). Hydrogen atoms (except water), CF_3SO_3^- , and one water molecule are omitted for clarity. Color code: ruthenium (purple), nitrogen (blue), oxygen (red), carbon (gray), and hydrogen (green).

the equatorial direction, and the two axial positions are occupied by one 1,3-dimethylimidazolium-2-ylidene and one aqua ligand. In both crystal structures the methyl groups of the NHC ligand are directed in the same direction. One methyl group is directed to the open side of the planar bda ligand, and the other is between the two pyridine rings of the bda ligand. Since in the ^1H NMR only a single peak can be seen for the methyl groups, it shows that the rotation of the mmi ligand around the $\text{Ru}-\text{C}(\text{mmi})$ bond in the solution is possible. Selected bond lengths and angles of the complex salts **2** and **3** are summarized in Table 1 and Supporting Information Table S1.

Table 1. Selected Bond Lengths and Angles for X-ray Crystal Structure of **2**

Bond Lengths (Å)		
Ru1–N1		1.979(2)
Ru1–N2		1.985(2)
Ru1–O1		2.044(1)
Ru1–O4		2.063(2)
Ru1–C13		2.024(2)
Ru1–O5		2.177(2)
O3...H9B		2.16(5)
Angles (deg)		
C13–Ru1–O5		171.01(8)
O1–Ru1–O4		126.45(7)
N1–Ru1–N2		77.71(8)
N3–C13–N4		105.1(2)

Counterions do not have significant influence on the coordination sphere around the ruthenium center in **2** and **3**. The distances between the ruthenium center and the nitrogen atoms of the bda ligand are similar (1.979(7)–1.987(2) Å) in **2** and **3**. They are a little longer, however, than those bonds (1.914–1.905 Å) of $[\text{Ru}^{\text{II}}(\text{bda})(\text{pic})_2]$ (**A**). The $\text{Ru}-\text{O}$ (carboxylate) bond distances of **2** and **3** (2.044(2)–2.063(1) Å) are considerably shorter than those in $[\text{Ru}^{\text{II}}(\text{bda})(\text{pic})_2]$ (2.172(7)–2.216(7) Å). This comes along with a slightly bigger angle of $\text{O}_1-\text{Ru}-\text{O}_2$ of **2** and **3** than that in $[\text{Ru}^{\text{II}}(\text{bda})(\text{pic})_2]$.

Apparently, there is a stronger Ru–O(carboxylate) interaction in **2** and **3**, compared to that of **A**, primarily because of a higher valent state of the ruthenium center (Ru^{III}) in **2** and **3**. The higher the valence of the ruthenium core is, the better the interaction of the atomic orbital of the metal and the carboxylate ligand. The trend is continued if the solid-state molecular structure of the seven-coordinate μ -(HOHOH)-[Ru^{IV}(bda)(pic)₂]₂(PF₆)₃ (**E**) is taken into consideration,²¹ where the distances between the ruthenium center and the oxygen atoms of the bda ligand are even shorter (2.033(2)–2.043(2) Å) and the angle of O₁–Ru–O₂ is more greatly expanded to 145.02(9)°.

The bond distance of Ru–C(mmi) in **2** and **3** (2.021(2)–2.024(2) Å) lies in the region of typical bond lengths between 1,3-dimethylimidazolium-2-ylidene and ruthenium in literature (1.967(5)–2.115(4) Å).^{38,39} The Ru–C(mmi) bond is a bit shorter than the Ru–N (4-picoline) bonds in [Ru^{II}(bda)(pic)₂] (2.070(6)–2.084(6) Å). The Ru–O(aqua) bond distances of **2** and **3** are relatively long, 2.177(2) Å and 2.164(2) Å, respectively, indicating weak coordination between Ru center and water in both cases.

Complex salt **2** was chosen as the target WOC for investigation in this Article due to its proper stability and solubility. Different from the previous examples of Ru-bda type WOCs (**A**–**C**) that possess two identical monodentate aromatic nitrogen ligands, **2** has a water molecule and a carbene (mmi) ligand at its axial positions. Apparently, the different ligand environment will influence the electronic structure at the metal center. Moreover, the carbene ligand is expected to interact with the metal center through a weak π -back-donating coordination, due to the vacant but conjugate p orbital at the NCN carbon. The different features of Ru-ligand coordinate bonds may influence the catalytic behavior of Ru-bda WOCs.

Electrochemical Study. First, the differential pulse voltammogram (DPV) of complex salt **2** was conducted in aqueous solutions with different pH values (1 < pH < 6; complex salt **2** decomposes in higher pH solutions than pH = 6). The DPV curve of **2** at pH = 1.0 is displayed in Figure 3b, in which one current peak is clearly visible at 0.52 V versus NHE and another peak is merely discernible at 1.23 V versus NHE. These two current signals are assigned to the oxidation processes of Ru^{II} → Ru^{III} and Ru^{III} → Ru^{IV}, respectively. In the CV curve of **2** at pH = 1.0, a reversible redox wave is observed at 0.48 V, but an irreversible wave is at 1.23 V. It indicates the involvement of a chemical process when **2** is oxidized to its tetravalent state. According to the theoretical study (*vide infra*), complex salt **2** could be oxidized to the Ru^V state at a potential of 1.33 V versus NHE. The Ru^{IV} → Ru^V redox current, however, might be too kinetically unfavorable to be distinguished in the potential sweep measurements. Current onset, corresponding to the catalytic water oxidation, emerged at about 1.5 V versus NHE in either the DPV or CV curve of **2** described above.

The Pourbaix diagram of complex salt **2** is shown in Figure 3c. Here the segments of different valent ruthenium species are divided by the redox potential versus pH lines. Valence of the ruthenium center and degree of protonation of the aqua ligand are marked for each ruthenium species in the diagram. The redox potential of the Ru^{II} to Ru^{III} process is independent of the pH value over the pH = 1–6 range, indicating that proton transfer is not involved in this redox process. However, the Ru^{III} to Ru^{IV} redox potential was observed to be linearly dependent

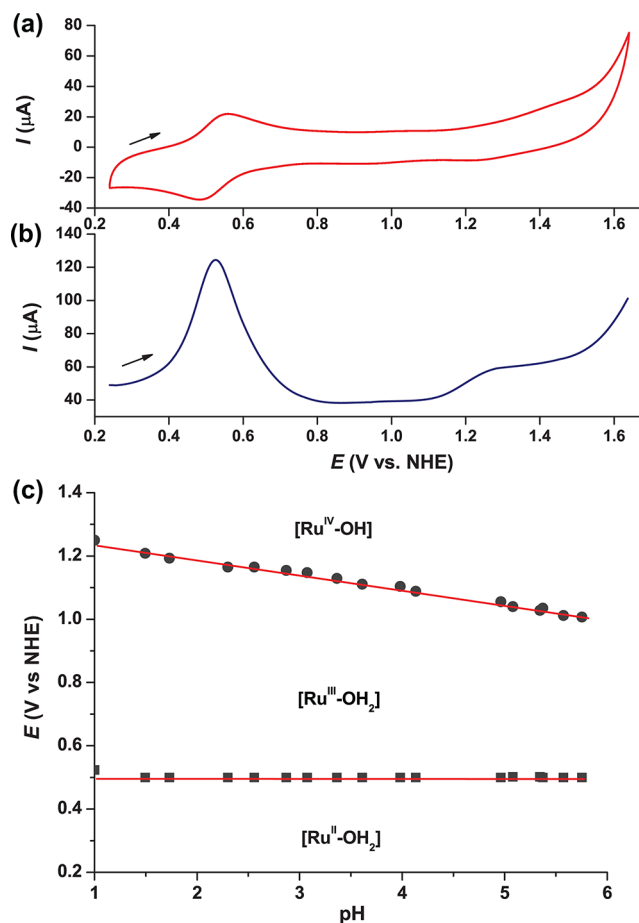
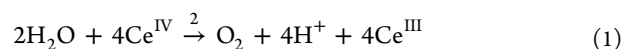


Figure 3. Upper: Cyclic voltammogram (a) and differential pulse voltammogram (b) of **2** in a pH 1.0 triflic acid aqueous solution. Bottom: Pourbaix diagram of **2** (c).

on the pH value with a slope of *ca.* 48 mV/pH. Consequently, we propose that the Ru^{III} to Ru^{IV} oxidation is a one proton-coupled one electron-transfer (PCET) process. The potential/pH slope deviates from that of a typical PCET process (59 mV/pH), probably because the Ru^{III} → Ru^{IV} redox wave, which we observed in the DPV curve of **2**, partially overlapped with the weak Ru^{IV} → Ru^V redox wave. According to the theoretical studies (*vide infra*), the Ru^{IV} → Ru^V oxidation of **2** is also a one proton-coupled one electron-transfer process that occurs at a redox potential merely 100 mV more positive than that of the Ru^{III} → Ru^{IV} process. On the basis of electrochemical measurements above and theoretical studies (*vide infra*), we conclude that, in the potential sweep upon **2** (from cathode to anode), it undergoes the following Ru^{II}–OH₂ → Ru^{III}–OH₂ → Ru^{IV}–OH → Ru^V=O oxidation sequence before the emergence of a current onset of catalytic water oxidation.

Catalytic O₂ Evolution. The catalytic activity of **2** for water oxidation was tested in acidic medium (0.1 M HNO₃, initial pH = 1.0) containing a large excess of Ce^{IV} (thousands of equivalents) which played the role of a one-electron acceptor. Oxygen generation was instantly detected by a pressure transducer as soon as complex salt **2** was injected into the acidic Ce^{IV} solution. The overall reaction of O₂ evolution can be described by eq 1 that includes multiple unit reactions.



The rate of O₂ evolution was attenuating as the catalytic reaction proceeded, due to decomposition of **2** under the harsh oxidation environment of Ce^{IV} solution. After about 10 min, the catalytic O₂ generation completely ceased. The amount of generated dioxygen was verified with a gas chromatography at the end-point of each experiment. It is found that the TON of **2** was influenced by its concentration present in the catalytic system. Under an optimized condition, a TON of 63 was achieved (Supporting Information Figure S3).

Preliminary analysis of the O₂ evolution catalyzed by **2** was carried out through a series of trials, in which the present concentration of **2** was changed but the initial concentration of Ce^{IV} was kept largely excess and constant (Figure 4). Under

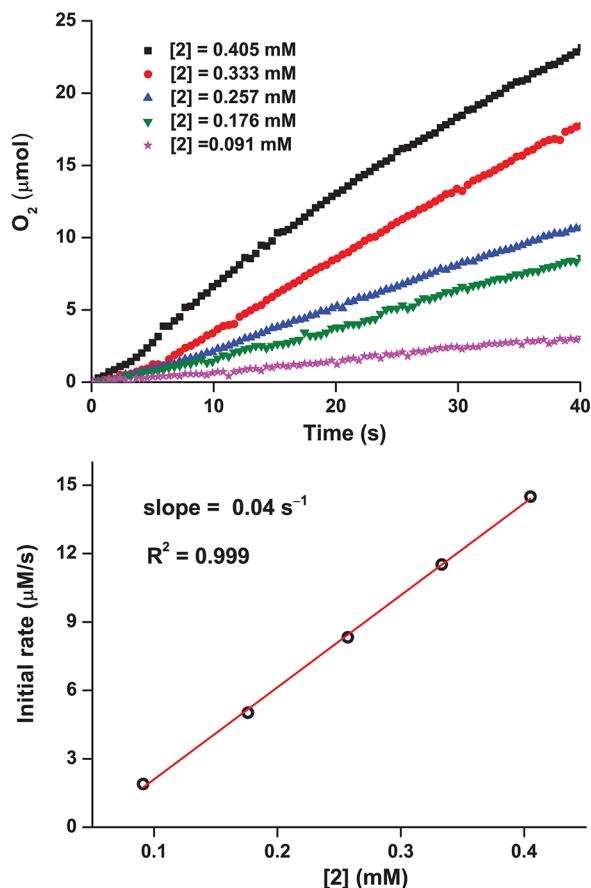


Figure 4. Upper: Initial phase of O₂ evolution versus time at various concentrations of **2**. Bottom: Initial rate of O₂ evolution versus concentration of **2**. The initial rate is calculated by linearly fitting the O₂ evolution versus time plots in the 0–40 s period.

such an experimental condition, the decay of concentration of Ce^{IV} is negligible during the incipient period of the catalytic reaction, and thus, the initial rate of O₂ generation is independent to the concentration of Ce^{IV}. As shown in Figure 4, the initial rate of O₂ evolution is linearly depending on the concentration of **2**, following a pseudo-first-order kinetics initial rate = $k_{O_2}[2]$. It is inferred that there is only a single Ru intermediate involved in the rate-determining step of the catalytic cycle under such experimental conditions. The rate constant of O₂ evolution k_{O_2} , which could also be defined as the TOF of **2**, was determined as 0.04 s⁻¹ (Figure 4, bottom). Compared to the analogous catalysts **A** (32 s⁻¹), **B** (303 s⁻¹), and **C** (286 s⁻¹) studied in our previous work, complex salt **2**

has a significant smaller catalytic activity toward water oxidation, as reflected by its TOF being smaller by several orders of magnitudes.²⁰ It is therefore necessary to investigate the processes leading to the observed catalytic activity in more detail.

Kinetics Study. In the typical experiments of O₂-evolution catalyzed by **2**, a large excess of Ce^{IV} salt was applied as the electron acceptor. Under such conditions, any reaction step involving Ce^{IV} is essentially fast insofar as the overall rate of catalysis is independent to the concentration of Ce^{IV}. In order to obtain more information about the kinetics of catalytic water oxidation by **2**, the reaction rate was further studied under conditions with relatively low Ce^{IV} concentrations (e.g., [Ce^{IV}] being tens of equivalents with respect to [**2**]). For the overall reaction expressed in eq 1, its rate is directly related to the rate-limiting step of the catalytic cycle and can be generally written as rate = $k_{cat}[Ce^{IV}]^m[2]^n$, where k_{cat} is the rate constant and m and n are the reaction orders in terms of the concentrations of Ce^{IV} and that of the catalyst. The determination of reaction orders was conducted by monitoring the rate of Ce^{IV} consumption in two series of experiments which applied a constant initial concentration of Ce^{IV} or **2** and variable concentrations of the other. Thus, the expression of reaction rate can be simplified in terms of the initial rate (reaction rate at time = 0), e.g., initial rate = $k[2]^n$ (constant initial [Ce^{IV}] = [Ce^{IV}]₀, and $k = k_{cat}[Ce^{IV}]_0^m$) or initial rate = $k'[Ce^{IV}]^m$ (constant initial [**2**] = [**2**]₀, and $k' = k_{cat}[2]_0^n$).

In the first series of experiments (Figure 5), the initial concentration of Ce^{IV} was kept constant ([Ce^{IV}]₀ = 1 mM), whereas the concentration of **2** was varied from 12 to 28 μM. The Ce^{IV} consumption in each experiment was monitored by following the absorbance change of Ce^{IV} at 360 nm (Figure 5, left). The initial rate of Ce^{IV} consumption, which is 4-fold the initial rate of water oxidation, was represented as the slope of tangent of the time-resolved absorbance trace at time = 0. In the realistic operation, the slope of tangent was approximated by linearly fitting the incipient segment (around 10 s) of the time-resolved absorbance curve. As showed in the initial rate versus [**2**] plot (Figure 5, right), the initial rate of Ce^{IV} consumption is first order with respect to **2**. The rate constant of Ce^{IV} consumption, estimated as the slope of the initial rate versus [**2**] plot, was $1.1 \times 10^3 \text{ M}^{-1} \text{ s}^{-1}$. Therefore, k_{cat} was estimated as $2.8 \times 10^2 \text{ M}^{-1} \text{ s}^{-1}$, a quarter of the rate constant of Ce^{IV} consumption, because evolution of each dioxygen involves transfer of four electrons to the electron acceptors. In the following series of experiments (Figure 6), the concentration of **2** ([**2**]₀ = 0.04 mM) was kept constant, while the concentration of Ce^{IV} was varied between 0.4 and 1.0 mM. It is found that the initial rate of Ce^{IV} consumption is linearly depending on the concentration of Ce^{IV} (Figure 6, right), indicating a first reaction order with respect to [Ce^{IV}]. The rate constant of catalytic water oxidation by **2**, $k_{cat} = 3.0 \times 10^2 \text{ M}^{-1} \text{ s}^{-1}$, was obtained from this series of experiments independently. By combining the results from the kinetics studies above, we concluded that, in the condition of relatively low Ce^{IV} concentrations, catalytic water oxidation by **2** is an overall second-order reaction formally, and its reaction rate can be described by eq 2. The rate constants k_{cat} calculated independently from the two series of kinetic measurements show quantitative consistence ($2.8 \times 10^2 \text{ M}^{-1} \text{ s}^{-1}$ and $3.0 \times 10^2 \text{ M}^{-1} \text{ s}^{-1}$, respectively). The small error involved in the measurement of k_{cat} drives from the following two aspects primarily. One is the approximation of the tangent at time = 0

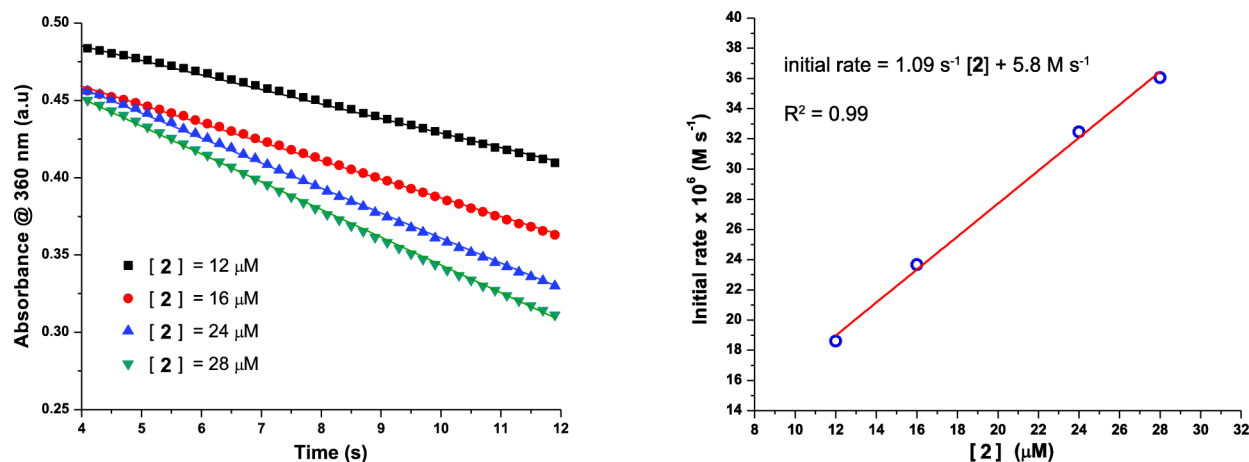


Figure 5. Left: Absorbance decay at 360 nm depending on different concentrations of **2**. Conditions: Initial [Ce^{IV}] = 1 mM (aqueous HNO₃ solution, pH = 1.0). Right: Initial rate of Ce^{IV} consumption versus [2]. The change of absorbance was transferred to the consumption of Ce^{IV} according to the Lambert–Beer law, $\Delta C = \Delta A / \epsilon b$ (ΔC is the change of Ce^{IV}, ΔA is the change of absorbance, ϵ is the molar extinction coefficient of Ce^{IV} which was measured as 500 M⁻¹ cm⁻¹ under this experimental conditions, and $b = 1$ cm is the path length of the absorption cuvette).

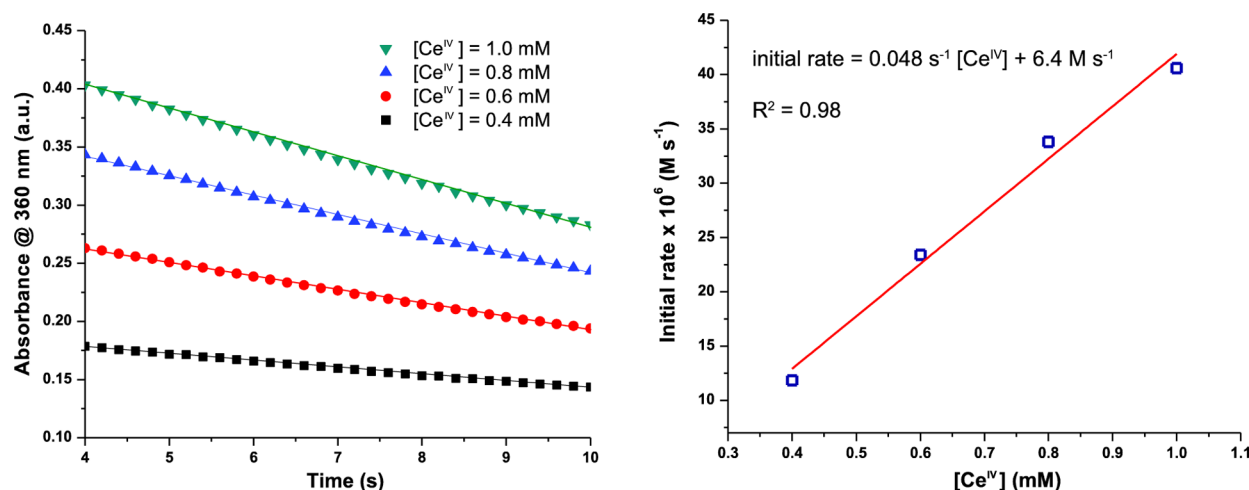


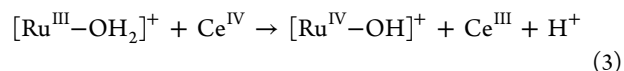
Figure 6. Left: Absorbance decay at 360 nm depending on different concentrations of Ce^{IV}. Conditions: Initial [2] = 0.04 mM (aqueous HNO₃ solution, pH = 1.0). Right: Initial rate of Ce^{IV} consumption versus [Ce^{IV}], the change of absorbance was transferred to the consumption of Ce^{IV} according to the same method described in the caption of Figure 5.

in the traces of Ce^{IV} absorbance decay. The other is truncation of the traces of Ce^{IV} absorbance decay before time = 4 s (Supporting Information Figure S4). In each trial of above Ce^{IV} consumption experiments, the absorbance of the reaction mixture at 360 nm barely changed in the first 2–4 s. Therefore, we propose that this period of time is primarily corresponding to a presteady state of catalysis, that is, conversion of the initial trivalent Ru species to the dominant Ru species in the catalytic cycle (reactant of the rate-determining state). Notably, the formal expression of the reaction rate law (eq 2) implies that, under the condition of relatively low Ce^{IV} concentrations, the rate-determining step of the catalytic cycle is associated to both Ce^{IV} and catalyst **2**.

$$\text{rate} = -4 \frac{d[\text{Ce}^{\text{IV}}]}{dt} = k_{\text{cat}}[\mathbf{2}][\text{Ce}^{\text{IV}}] \quad (2)$$

Stopped-flow UV–vis experiments were performed to explore the kinetics of individual steps involved in the catalytic cycle of water oxidation by **2**. By addition of equimolar Ce^{IV} to **2** in pH 1.0 HNO₃ solution, the complex was rapidly oxidized to the tetravalent [Ru^{IV}(bda)(mmi)(OH₂)OH]⁺ ([Ru^{IV}–

OH]⁺) species via a PCET process (eq 3), which was illustrated by the Pourbaix diagram of **2** (*vide supra*). The geometry of [Ru^{IV}–OH]⁺ is delineated in detail in the Theoretical Study section below. Correspondingly, time-resolved absorbance traces of the mixture exhibited dramatically fast drop over a wide range of wavelength (Figure 7, upper), for instance, at wavelength = 308 nm (Figure 7, bottom). Rate of the PCET step is first order in the concentration of Ce^{IV} as well as that of **2** (second order overall), following the rate law described in eq 4. The rate constant of this step $k_1 = 6.5 \times 10^5$ M⁻¹ s⁻¹ was determined by simulating the drop of the absorbance at 308 nm (Figure 7, bottom) according to eq 5, which is the integration form of the rate law (eq 4) correlated to the absorbance change (A , A_0 , and A_∞ represent absorbance value of the sample at time t , 0, and infinity, respectively).



$$-\frac{d[\text{Ru}^{\text{III}}]}{dt} = k_1[\text{Ru}^{\text{III}}][\text{Ce}^{\text{IV}}] = k_1[\text{Ru}^{\text{III}}]^2 \quad (4)$$

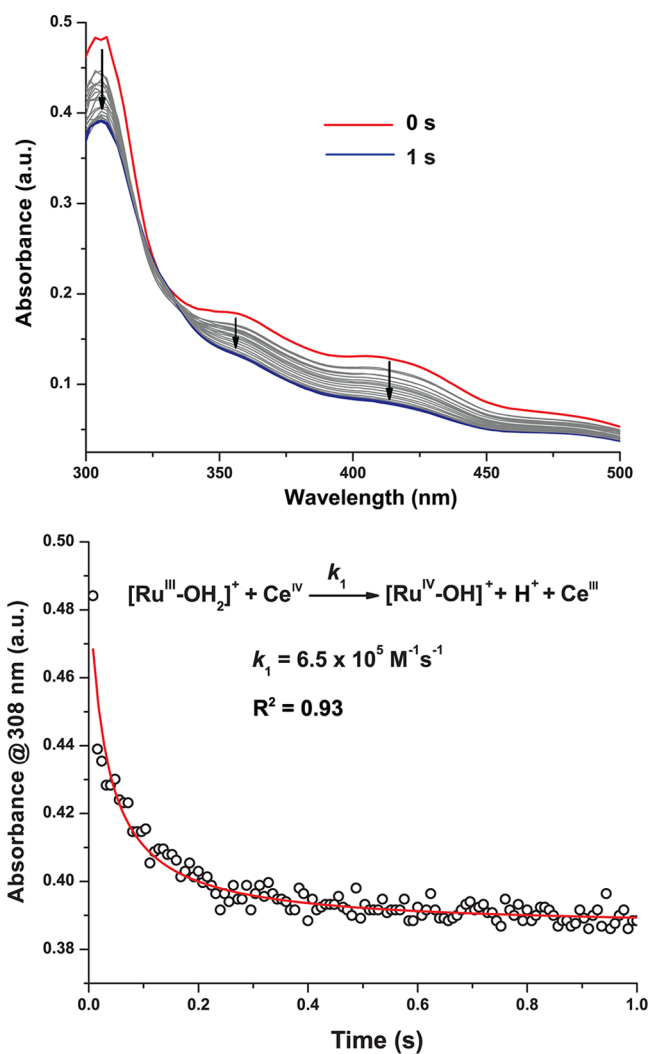
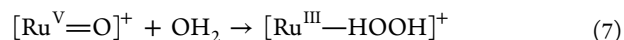
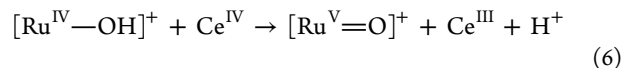


Figure 7. Upper: Change of the absorbance spectra (0–1 s) after mixing **2** with 1 equiv of Ce^{IV} . Conditions: pH = 1.0 HNO_3 solution, $[\text{2}] = 0.05 \text{ mM}$. Bottom: Fitting of the absorbance change at 308 nm according to the reaction law.

$$\frac{(A_0 - A_\infty)}{[\text{Ru}^{\text{III}}]_0(A - A_\infty)} = k_1 t + \frac{1}{[\text{Ru}^{\text{III}}]_0} \quad (5)$$

Addition of another equivalent of Ce^{IV} to the resulting $[\text{Ru}^{\text{IV}}\text{—OH}]^+$ solution led to a biphasic process of absorbance change versus time (Figure 8a). The trace of absorbance change at wavelength = 308 nm, for example, exhibits an initial rapid drop within the first several seconds in the time window of observation. This drop is followed by a slow recovery of absorbance which eventually reaches a plateau after around 80 s, signifying reaction completion (Figure 8b). The initial phase of the absorption change is corresponding to the oxidation of $[\text{Ru}^{\text{IV}}\text{—OH}]^+$ to the $[\text{Ru}^{\text{V}}(\text{bda})(\text{mmi})(\text{OH}_2)=\text{O}]^+$ ($[\text{Ru}^{\text{V}}=\text{O}]^+$) species (eq 6). The geometry of $[\text{Ru}^{\text{V}}=\text{O}]^+$ is delineated in detail in the Theoretical Study section below. This PCET step is a second-order reaction that also conforms to the rate law described in eq 5. The subsequent phase of absorbance change in the 3–80 s time course is consistent with the model of a water molecule acting as a nucleophile, which is attacking the oxo group of $[\text{Ru}^{\text{V}}=\text{O}]^+$ and yielding $[\text{Ru}^{\text{III}}(\text{bda})(\text{mmi})\text{—HOOH}]^+$ ($[\text{Ru}^{\text{III}}\text{—HOOH}]^+$) as a product (eq 7, the structure of $[\text{Ru}^{\text{III}}\text{—HOOH}]^+$ is delineated in detail in the Theoretical

Study section below).²⁶ This O—O bond formation step is a pseudo-first-order reaction in the given aqueous solution where the concentration of water is enormous. Rate constants of $[\text{Ru}^{\text{IV}}\text{—OH}]^+ \rightarrow [\text{Ru}^{\text{V}}=\text{O}]^+$ (k_2) and $[\text{Ru}^{\text{V}}=\text{O}]^+ \rightarrow [\text{Ru}\text{—HOOH}]^+$ ($k_{\text{O-O}}$) steps were calculated as $5.6 \times 10^3 \text{ M}^{-1} \text{ s}^{-1}$ and $7.6 \times 10^{-2} \text{ s}^{-1}$, respectively, by global fitting according to the proposed $[\text{Ru}^{\text{IV}}\text{—OH}]^+ \rightarrow [\text{Ru}^{\text{V}}=\text{O}]^+ \rightarrow [\text{Ru}\text{—HOOH}]^+$ process (Figure 8b). Distribution of Ru-containing species and their spectra are also displayed in Figure 8c,d.



Rate constants measured in this section were compiled in Table 2. It should be noted that they are measured at different ratios of concentration between Ce^{IV} and **2**. For the measurement of k_{O_2} , the concentration of Ce^{IV} was in large excess (thousands of equivalents with respect to **2**); for k_{cat} , concentration of Ce^{IV} was mildly excess (tens of equivalents); and in the measurements of k_1 and k_2 , Ce^{IV} was added in stoichiometry.

k_{cat} represents the rate constant of the rate-determining step, in which Ce^{IV} participates as a reactant. Because either k_1 or k_2 is much greater than k_{cat} , neither the $[\text{Ru}^{\text{III}}] \rightarrow [\text{Ru}^{\text{IV}}\text{—OH}]^+$ nor the $[\text{Ru}^{\text{IV}}\text{—OH}]^+ \rightarrow [\text{Ru}^{\text{V}}=\text{O}]^+$ elementary reaction is the rate-determining step in the catalytic cycle of water oxidation by **2**. These experimental data point out that further oxidation of $[\text{Ru}^{\text{III}}\text{—HOOH}]^+$ species to a tetravalent or pentavalent Ru-peroxo intermediate is the slowest step in the catalytic cycle.^{8,40} Rate constant of this step approximates to the value of k_{cat} . Under the condition of sufficiently high concentration of Ce^{IV} , however, the reaction rate of Ce^{IV} -involved rate-determining step is accelerated to such an extent that it is faster than the rate of the nucleophile attack of the water molecule (pseudo-first-order). Thus, the water attacking step, whose rate is not influenced by the concentration of Ce^{IV} , became slowest in the catalytic cycle. Rate constant of O_2 generation ($k_{\text{O}_2} = 4.0 \times 10^{-2} \text{ s}^{-1}$), which was assigned in the presence of high concentration of Ce^{IV} , has a value close to the rate constant of the nucleophile attack of the water molecule ($k_{\text{o-o}} = 7.6 \times 10^{-2} \text{ s}^{-1}$). This result agrees with our description here about the shift of rate-limiting steps under different conditions. On the basis of the presented data several important steps in the catalytic mechanism can be described. However, with respect to other Ru-bda based WOCs, the question of whether a seven-coordinate species occurs during the catalysis remains open.

Theoretical Study. Density functional theory (DFT) calculations have helped us to understand the catalytic behaviors of Ru-bda complexes in our previous work.^{23,27,41} The purpose of the theoretical study here is to explore the configurations of intermediates and energetics of unit reactions involved in the catalytic water oxidation pathway. In order to describe the surroundings of the aqueous medium accurately, an explicit water molecule was included as an acceptor of hydrogen bonding for each polar hydrogen (aqua or hydroxyl group) when the geometry of ruthenium intermediates was simulated.

The optimized structure of **2** (Supporting Information Figure S6) shows all features observed in its crystal structure, with slightly longer Ru—O(carboxylate) bonds (2.057–2.102 Å). The divalent state of **2** (denoted as $\text{Ru}^{\text{II}}\text{—OH}_2$) was also simulated, and its calculated structure is shown in Supporting

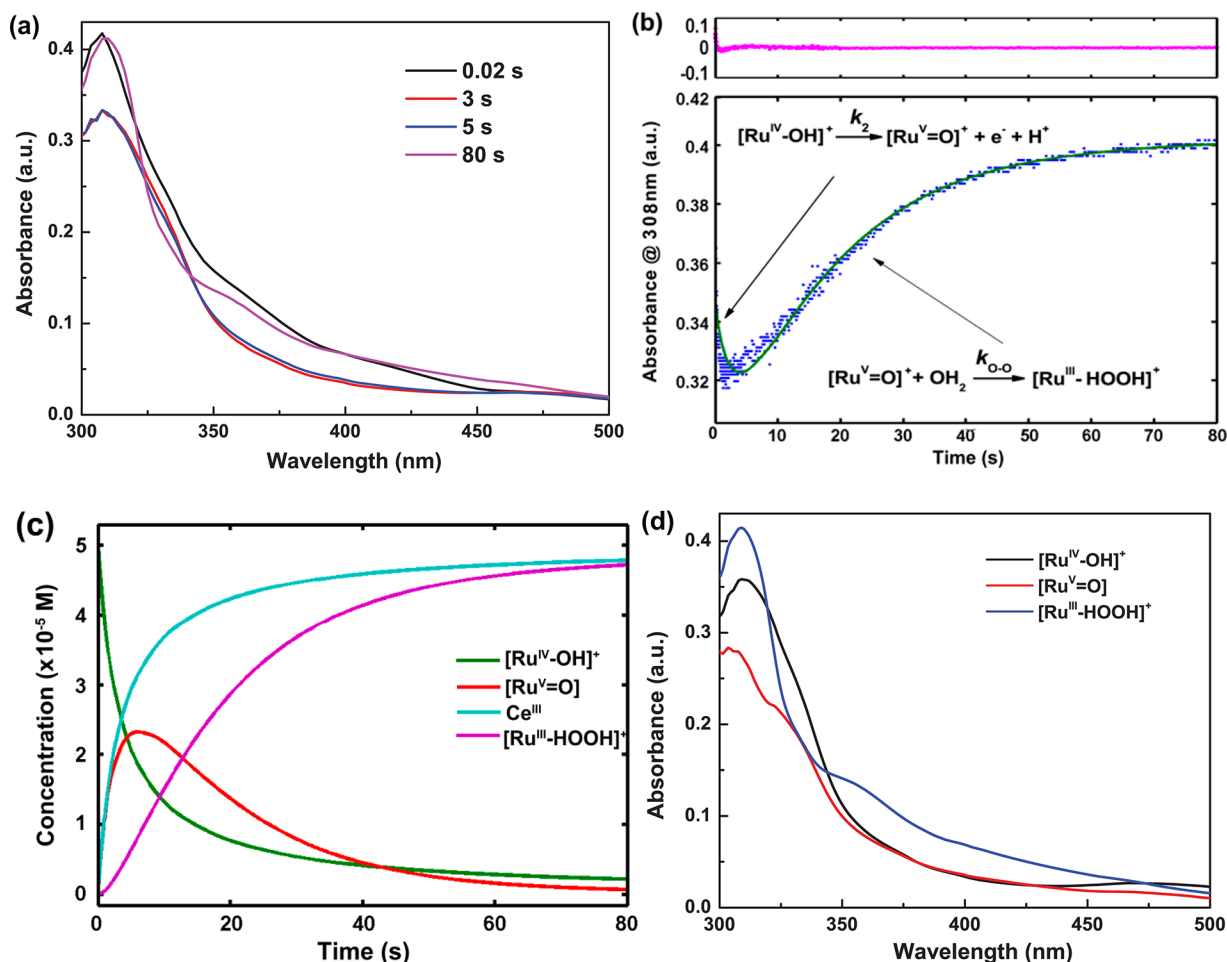


Figure 8. Kinetic and spectral data for the generation of $[\text{Ru}^{\text{V}}\text{=O}]^+$ species and O—O bond formation steps. (a) Selected absorbance spectra at certain reaction time after addition of 1 equiv of Ce^{IV} to $[\text{Ru}^{\text{IV}}\text{-OH}]^+$ in aqueous HNO_3 solution, pH = 1.0. (b) Kinetic trace (blue dots) and fitting line (green) at wavelength = 308 nm including the residues (pink). (c) Distribution diagram of reactants and intermediates. (d) Calculated spectra of Ru-containing species according to global fitting performed by ReactLab.

Table 2. Rate Constants Involved in the Water Oxidation Catalyzed by **2**

rate constant (20 °C)	reaction description
$k_{\text{O}_2} = 4.0 \times 10^{-2} \text{ s}^{-1}$	eq 1
$k_{\text{cat}} = 2.8\text{--}3.0 \times 10^2 \text{ M}^{-1} \text{ s}^{-1}$	eq 1
$k_1 = 6.5 \times 10^5 \text{ M}^{-1} \text{ s}^{-1}$	eq 3
$k_2 = 5.6 \times 10^3 \text{ M}^{-1} \text{ s}^{-1}$	eq 6
$k_{\text{o-o}} = 7.6 \times 10^{-2} \text{ s}^{-1}$	eq 7

Information Figure S5. Due to steric repulsion, both the aqua and mmi ligands of $\text{Ru}^{\text{II}}\text{-OH}_2$ tilt toward the open O—Ru—O cleft formed by the coordination between bda and Ru center, leading to a smaller O(aqua)—Ru—C(mmi) angle of 168.7° compared to that of **2**. The ^1H NMR spectrum obtained for the reduction of **2** *in situ*, however, showed only one singlet peak for both CH_3 substituents of the mmi ligand. This ^1H NMR investigation suggests therefore a very low energy barrier for the rotation of $\text{Ru}(\text{II})\text{-C}(\text{mmi})$ bond. The redox potential of $\text{Ru}^{\text{II}}\text{-OH}_2$ (**2**) was calculated to be 0.49 V versus NHE, which

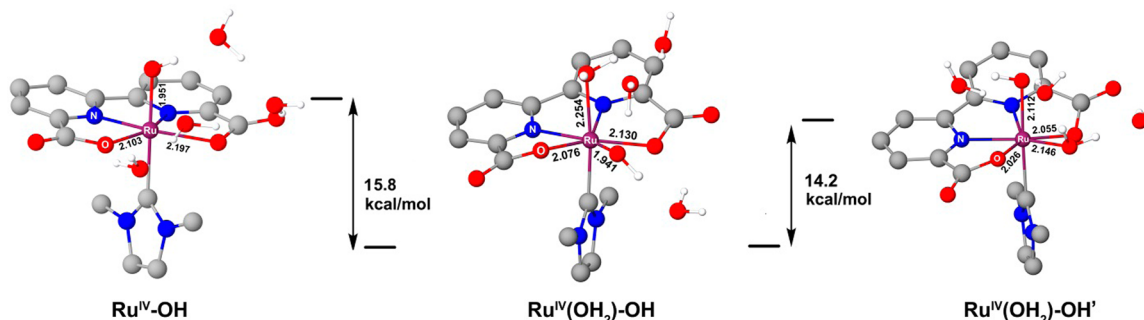


Figure 9. Optimized structures and relative energies for Ru^{IV} intermediates. Non-OH hydrogens are not displayed for clarity. All distances are in Å.

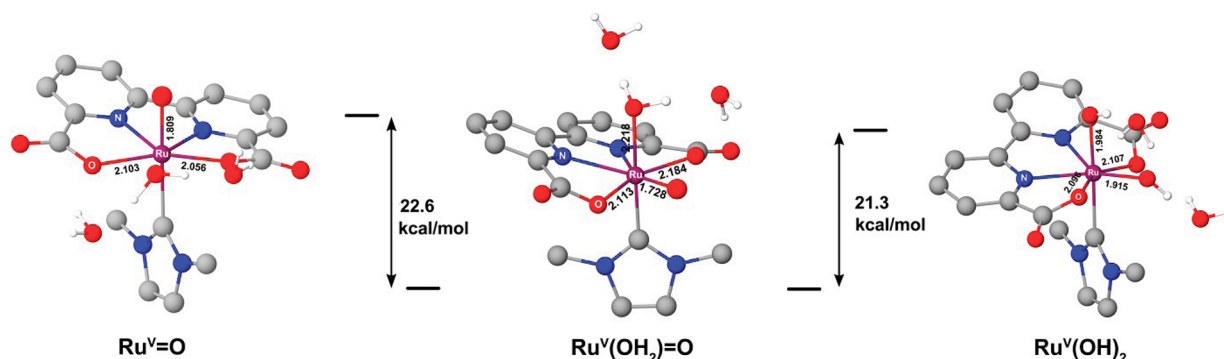


Figure 10. Optimized structures and relative energies for Ru^{V} intermediates. Non-OH hydrogens are not displayed for clarity. All distances are in Å.

is in excellent agreement with the experimental value (0.48 V, see the Electrochemical Study section above).

Further oxidation of **2** undergoing PCET process at 1.23 V versus NHE results in a Ru^{IV} species. This redox event has been disclosed in the Electrochemical Study section. We optimized three plausible configurations of this Ru^{IV} intermediate, including six- and seven-coordinate Ru^{IV} candidates, and compared their free Gibbs energies relatively (Figure 9). The most favored structure was the seven-coordinate Ru^{IV} configuration denoted as $\text{Ru}^{\text{IV}}(\text{OH}_2)\text{—OH}$, in which an aqua ligand is located at the *trans* position to the *mmi* ligand and a hydroxyl ligand is in the same plane of the *bda* ligand. The calculated free energy of the seven-coordinate species $\text{Ru}^{\text{IV}}(\text{OH}_2)\text{—OH}$ is 15.8 kcal/mol lower than that of the six-coordinate Ru^{IV} configuration denoted as $\text{Ru}^{\text{IV}}\text{—OH}$, and 14.2 kcal/mol lower than that of another seven-coordinate Ru^{IV} configuration denoted as $\text{Ru}^{\text{IV}}(\text{OH}_2)\text{—OH}'$, where the hydroxyl group occupies the *trans* position of the *mmi* ligand and the aqua ligand lies in the equatorial plane. While the triplet state of $\text{Ru}^{\text{IV}}\text{—OH}$ is more favored, both seven-coordinate Ru^{IV} configurations have singlet ground states. The dominance of seven-coordinate $\text{Ru}^{\text{IV}}(\text{OH}_2)\text{—OH}$ herein can be interpreted in two ways. First, the seven-coordinate species $\text{Ru}^{\text{IV}}(\text{OH}_2)\text{—OH}$ is a formal 18-electron complex while the six-coordinate species $\text{Ru}^{\text{IV}}\text{—OH}$ is a formal 16-electron complex. Second, the flexibility of *bda* ligand and the big O(carboxylate)—Ru—O(carboxylate) angle of **2** makes it possible to form a seven-coordinate species without any additional strain in the ligands.^{21,25} The calculated redox potential of $2 \rightarrow \text{Ru}^{\text{IV}}(\text{OH}_2)\text{—OH}$ process (1.22 V vs NHE) is extremely close to the experimental data. It validates the high accuracy of our current computational approach for reproducing the geometries of intermediates and predicting the energetics of the reactions.

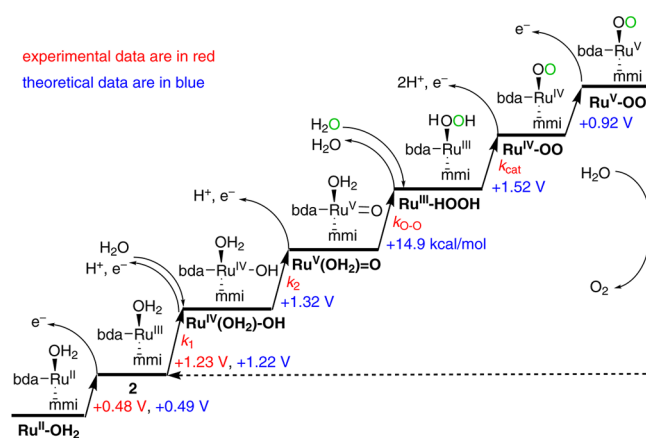
Removal of one electron from $\text{Ru}^{\text{IV}}(\text{OH}_2)\text{—OH}$ may couple with proton transfer from the aqua or hydroxyl ligands of $\text{Ru}^{\text{IV}}(\text{OH}_2)\text{—OH}$ and dissociation of the aqua ligand, leading to three possible Ru^{V} configurations illustrated in Figure 10. Our calculated results indicate that the formally seven-coordinate $[\text{Ru}^{\text{V}}=\text{O}]^+$ species, $\text{Ru}^{\text{V}}(\text{OH}_2)=\text{O}$, is the dominant product. The free energy of $\text{Ru}^{\text{V}}(\text{OH}_2)=\text{O}$ with the oxo group in the equatorial position is 22.6 kcal/mol lower than that of $\text{Ru}^{\text{V}}=\text{O}$ and 21.3 kcal/mol lower than $\text{Ru}^{\text{V}}(\text{OH})_2$. The calculated potential of the $\text{Ru}^{\text{V}}(\text{OH}_2)=\text{O}/\text{Ru}^{\text{IV}}(\text{OH}_2)\text{—OH}$ redox couple is 1.32 V versus NHE which is merely 100 mV more positive than that of the $\text{Ru}^{\text{IV}}(\text{OH}_2)\text{—OH}_2$ couple. This small discrepancy between redox potentials might result in the overlap of current waves when a potential sweep measurement

was conducted upon the sequential $2 \rightarrow \text{Ru}^{\text{IV}}(\text{OH}_2)\text{—OH} \rightarrow \text{Ru}^{\text{V}}(\text{OH}_2)=\text{O}$ processes during the electrochemical experiments.

Once the $[\text{Ru}^{\text{V}}=\text{O}]^+$ state is reached, O—O bond formation reaction could occur by water nucleophilic attack to the Ru^{V} -oxo moiety, yielding a $[\text{Ru}^{\text{III}}\text{—HOOH}]^+$ species ($\text{p}K_{\text{a}1} = 10.7$, Supporting Information Figures S7 and S8). While transition state structures of this water nucleophilic attack process remain to be identified, our preliminary calculation shows that the reaction is endergonic by 14.9 kcal/mol. This $[\text{Ru}^{\text{III}}\text{—HOOH}]^+$ species could be oxidized to a formal $[\text{Ru}^{\text{IV}}\text{—OO}]$ (Supporting Information Figure S9) and then a formal $[\text{Ru}^{\text{V}}\text{—OO}]$ (Supporting Information Figure S10) species at an oxidation potential of 1.52 and 0.92 V, respectively.

Description of the Catalytic Cycle. On the basis of the combined experimental and theoretical results above, we present a complete picture for the catalytic cycle of water oxidation by **2** (Scheme 4), including available rate constants,

Scheme 4. Free Energy Diagram for the Catalytic Cycle of Water Oxidation by **2**^a



^a All data are measured or simulated at pH = 1 and room temperature.

redox potentials, and energy changes for all steps. The initial stage of the cycle is a sequence of two PCET reactions, through which complex salt **2** is oxidized to $\text{Ru}^{\text{V}}(\text{OH}_2)=\text{O}$. The following O—O bond formation step is extremely intricate, because it very likely proceeds in concert with proton transfer and ligand dissociation from the Ru center, for example the dissociation of aqua group. Furthermore, a hydrogen-bonding network around the Ru species might play an important role in the process.^{25,41} As a consequence, there are quite a few

plausible transition states and resulting configurations which deserve deeper and more careful analysis. According to the preliminary results from our current study, we propose that the water nucleophilic attack undergoes an intermolecular pathway rather than an intramolecular one, because of the following: (i) aqua and oxo ligands are both in rigid positions and the distance between them is quite far in the optimized structure of $\text{Ru}^{\text{V}}(\text{OH}_2)=\text{O}$; (ii) there is not such an orientation that the sp^3 orbital of available lone pair at aqua ligand can effectively overlap with the vacant π^* orbital of the $\text{Ru}^{\text{V}}=\text{O}$ moiety.

Oxygen evolution entails three further steps following the generation of hydroperoxo intermediate $\text{Ru}^{\text{III}}-\text{HOOH}$.^{7,24} First, $\text{Ru}^{\text{III}}-\text{HOOH}$ is oxidized to a formally peroxidic Ru^{IV} species $\text{Ru}^{\text{IV}}-\text{OO}$, in which the peroxo ligand is predicted by our DFT calculation to have a η^1 -coordinated geometry and a triplet electronic structure (Supporting Information Figure S9). The bond length of the peroxo group is 1.27 Å, much shorter than the covalent radius of an O–O single bond. Thereby, it is more appropriate to say that the ruthenium center of $\text{Ru}^{\text{IV}}-\text{OO}$ contains a charge of plus two formally and the peroxo group has a bond order of two, if valence bond theory is applied to express the distribution of electron density. Second, one electron is transferred from $\text{Ru}^{\text{IV}}-\text{OO}$ to the Ce^{IV} oxidant, resulting in the generation of a formal Ru^{V} peroxo intermediate denoted as $\text{Ru}^{\text{V}}-\text{OO}$ (Supporting Information Figure S10). It also favors a η^1 -coordinated peroxidic group with a bond length of 1.21 Å that is considerably shorter than that of the peroxo group in $\text{Ru}^{\text{IV}}-\text{OO}$ and almost equals to the bond length of a free dioxygen molecule. Finally, the O_2 ligand of $\text{Ru}^{\text{V}}-\text{OO}$ is exchanged by a solvent water molecule, leading to the evolution of dioxygen and close of the catalytic cycle.

Both the $\text{Ru}^{\text{III}}-\text{HOOH} \rightarrow \text{Ru}^{\text{IV}}-\text{OO}$ and $\text{Ru}^{\text{IV}}-\text{OO} \rightarrow \text{Ru}^{\text{V}}-\text{OO}$ oxidations are spontaneous in the presence of Ce^{IV} whose redox potential is 1.75 V versus NHE given the reaction conditions in our experiment.⁴² Nevertheless, it should be noted that in our theoretical model the redox potential of the former reaction (1.52 V) is much more positive than that of the latter one (0.92 V). Hence, we believed that a higher energy barrier is required to overcome the former redox step rather than the latter one. Under catalytic conditions with relatively low concentration of Ce^{IV} , the rate of O_2 evolution (a quarter of the rate of Ce^{IV} consumption) is determined by this $\text{Ru}^{\text{III}}-\text{HOOH} \rightarrow \text{Ru}^{\text{IV}}-\text{OO}$ oxidation step. The rate constant of the overall water oxidation reaction, k_{cat} , equals the rate constant of the $\text{Ru}^{\text{III}}-\text{HOOH} \rightarrow \text{Ru}^{\text{IV}}-\text{OO}$ step. When the concentration of Ce^{IV} increases, the rate of the $\text{Ru}^{\text{III}}-\text{HOOH} \rightarrow \text{Ru}^{\text{IV}}-\text{OO}$ step will be significantly enhanced, and as a result, the O–O bond formation step tends to become the rate-limiting step of the catalytic cycle.

CONCLUSIONS

In conclusion, a novel ruthenium complex $[\text{Ru}^{\text{III}}(\text{bda})(\text{mmi})(\text{OH}_2)](\text{CF}_3\text{SO}_3)$ (**2**) was prepared as the latest member in the Ru-bda series of mononuclear water oxidation catalysts. Unlike the previous example of Ru-bda WOCs (**A–C**) that coordinates with two identical N donors as axial ligands, complex **2** contains an aqua and a carbene (mmi) ligand at its axial positions. Our study identified that **2** and other Ru-bda WOCs exhibited some similar features in their water oxidation catalysis. When oxidized to tetravalent state, complex salt **2**, as well as WOC **A–C**, forms a seven-coordinate Ru^{IV} -hydroxyl species which could be further oxidized to a seven-coordinate Ru^{V} -oxo intermediate. However, **2** proceeds through O–O

bond formation through a water nucleophilic attack pathway that is completely different from the bimolecular coupling pathway proposed for other reported Ru-bda WOCs. In brief, the change of axial ligands totally alters the catalytic mechanism of Ru-bda complexes. This strong ligand effect is putatively ascribed to the shift of SOMO levels depending on the electronic properties of different ligands and the role of aqua group as an internal base that draws solvent water molecules close to the Ru^{V} -oxo species. These findings here also provide new proof to corroborate our previous tentative conclusion that a typical Ru-bda type WOC (**A–C**) cannot keep high efficiency of catalyzing water oxidation through the coupling pathway, if one of its N donor ligands is replaced by water during the reaction.^{20,27} In all, our work helps with understanding the correlations between coordinate environment and the catalytic mechanism of mononuclear WOCs, which is crucial for the design and synthesis of next generation catalysts with high efficiency and great durability. On the basis of the presented findings it seems possible to modify the catalytic activity by introducing a modified NHC ligand. A change of the residues at the nitrogen atoms of the imidazole will have great influence on the accessibility of the seventh coordination site and can also influence the stability of the intermediates arising during catalysis. In addition, the free position on the imidazole backbone allows an extension of the ligand, which will have influence on the electronic structure at the donating C-atom of the NHC.

ASSOCIATED CONTENT

Supporting Information

Additional figures and tables. Crystallographic data in CIF format. This material is available free of charge via the Internet at <http://pubs.acs.org>.

AUTHOR INFORMATION

Corresponding Author

*E-mail: sven.rau@uni-ulm.de.

Author Contributions

[#]These authors contributed equally to this work.

Notes

The authors declare no competing financial interest.

ACKNOWLEDGMENTS

R.S. thanks the Elitenetzwerk Bayern and the DFG Research Training Group 1626 and the Graduate School Molecular Science Erlangen for financial support and inspiring discussions, and Ivana Ivanović-Burmazović from Department of Chemistry and Pharmacy, Chair of Bioinorganic Chemistry, FAU Friedrich-Alexander-Universität Erlangen-Nürnberg, for support.

We thank Dr. Rocío Sánchez and Mr. Ying Wang from Department of Theoretical Chemistry & Biology, School of Biotechnology, KTH Royal Institute of Technology, for their assistance in the theoretical study, and the China Scholarship Council (CSC), the National Natural Science Foundation of China (21120102036), the National Basic Research Program of China (2009CB220009 and 2014CB239402), the Swedish Energy Agency, the K&A Wallenberg Foundation, and the CMST COST Action CM1202 for financial support.

■ REFERENCES

- (1) Lewis, N. S.; Nocera, D. G. *Proc. Natl. Acad. Sci. U.S.A.* **2006**, *103*, 15729–15735.
- (2) Lewis, N. *Science* **2007**, 798–801.
- (3) Armaroli, N.; Balzani, V. *Angew. Chem., Int. Ed.* **2007**, *46*, 52–66.
- (4) Cook, T. R.; Dogutan, D. K.; Reece, S. Y.; Surendranath, Y.; Teets, T. S.; Nocera, D. G. *Chem. Rev.* **2010**, *110*, 6474–6502.
- (5) Barber, J. *Chem. Soc. Rev.* **2009**, *38*, 185–196.
- (6) Renger, G. *Curr. Sci.* **2010**, *98*, 1305–1319.
- (7) Concepcion, J. J.; Jurss, J. W.; Templeton, J. L.; Meyer, T. J. *J. Am. Chem. Soc.* **2008**, *130*, 16462–16463.
- (8) Romain, S.; Vigara, L.; Llobet, A. *Acc. Chem. Res.* **2009**, *42*, 1944–1953.
- (9) Concepcion, J. J.; Jurss, J. W.; Brennaman, M. K.; Hoertz, P. G.; Patrocinio, A. O. T.; Murakami Iha, N. Y.; Templeton, J. L.; Meyer, T. *J. Acc. Chem. Res.* **2009**, *42*, 1954–1965.
- (10) Kaveevivitchai, N.; Zong, R.; Tseng, H.-W.; Chitta, R.; Thummel, R. P. *Inorg. Chem.* **2012**, *51*, 2930–2939.
- (11) Lalrempuia, R.; McDaniel, N. D.; Müller-Bunz, H.; Bernhard, S.; Albrecht, M. *Angew. Chem., Int. Ed.* **2010**, *49*, 9765–9768.
- (12) Blakemore, J. D.; Schley, N. D.; Balcells, D.; Hull, J. F.; Olack, G. W.; Incarvito, C. D.; Eisenstein, O.; Brudvig, G. W.; Crabtree, R. H. *J. Am. Chem. Soc.* **2010**, *132*, 16017–16029.
- (13) Karlsson, E. A.; Lee, B.-L.; Åkermark, T.; Johnston, E. V.; Kärkäs, M. D.; Sun, J.; Hansson, Ö.; Bäckvall, J.-E.; Åkermark, B. *Angew. Chem., Int. Ed.* **2011**, *50*, 11715–11718.
- (14) Mullins, C. S.; Pecoraro, V. L. *Coord. Chem. Rev.* **2008**, *252*, 416–443.
- (15) Dogutan, D. K.; McGuire, R.; Nocera, D. G. *J. Am. Chem. Soc.* **2011**, *133*, 9178–9180.
- (16) Yin, Q.; Tan, J. M.; Besson, C.; Geletii, Y. V.; Musaev, D. G.; Kuznetsov, A. E.; Luo, Z.; Hardcastle, K. I.; Hill, C. L. *Science* **2010**, *328*, 342–345.
- (17) Ellis, W. C.; McDaniel, N. D.; Bernhard, S.; Collins, T. J. *J. Am. Chem. Soc.* **2010**, *132*, 10990–10991.
- (18) Fillol, J. L.; Codolá, Z.; Garcia-Bosch, I.; Gómez, L.; Pla, J. J.; Costas, M. *Nat. Chem.* **2011**, *3*, 807–813.
- (19) Duan, L.; Tong, L.; Xu, Y.; Sun, L. *Energy Environ. Sci.* **2011**, *4*, 238–244.
- (20) Duan, L.; Bozoglian, F.; Mandal, S.; Stewart, B.; Privalov, T.; Llobet, A.; Sun, L. *Nat. Chem.* **2012**, *4*, 418–423.
- (21) Duan, L.; Fischer, A.; Xu, Y.; Sun, L. *J. Am. Chem. Soc.* **2009**, *131*, 10397–10399.
- (22) Duan, L.; Wang, L.; Inge, A. K.; Fischer, A.; Zou, X.; Sun, L. *Inorg. Chem.* **2013**, *52*, 7844–7852.
- (23) Wang, L.; Duan, L.; Stewart, B.; Pu, M.; Liu, J.; Privalov, T.; Sun, L. *J. Am. Chem. Soc.* **2012**, *134*, 18868–80.
- (24) Polyansky, D. E.; Muckerman, J. T.; Rochford, J.; Zong, R.; Thummel, R. P.; Fujita, E. *J. Am. Chem. Soc.* **2011**, *133*, 14649–14665.
- (25) Tong, L.; Duan, L.; Xu, Y.; Privalov, T.; Sun, L. *Angew. Chem., Int. Ed.* **2011**, *50*, 445–449.
- (26) Concepcion, J. J.; Tsai, M.-K.; Muckerman, J. T.; Meyer, T. J. *J. Am. Chem. Soc.* **2010**, *132*, 1545–1557.
- (27) Duan, L.; Moyses, C.; Ahlquist, M. S. G.; Sun, L. *Proc. Natl. Acad. Sci. U.S.A.* **2012**, *109*, 15584–15588.
- (28) Garber, T.; Van Wallendael, S.; Rillema, D. P.; Kirk, M.; Hatfield, W. E.; Welch, J. H.; Singh, P. *Inorg. Chem.* **1990**, *29*, 2863–2868.
- (29) Becke, A. D. *J. Chem. Phys.* **1993**, *98*, 5648–5652.
- (30) Lee, C.; Yang, W.; Parr, R. G. *Phys. Rev. B* **1988**, *37*, 785–789.
- (31) Zhao, Y.; Truhlar, D. *Theor. Chem. Acc.* **2008**, *120*, 215–241.
- (32) Martin, J. M. L.; Sundermann, A. *J. Chem. Phys.* **2001**, *114*, 3408–3420.
- (33) Marten, B.; Kim, K.; Cortis, C.; Friesner, R. A.; Murphy, R. B.; Ringnalda, M. N.; Sitkoff, D.; Honig, B. *J. Phys. Chem.* **1996**, *100*, 11775–11788.
- (34) Tissandier, M. D.; Cowen, K. A.; Feng, W. Y.; Gundlach, E.; Cohen, M. H.; Earhart, A. D.; Coe, J. V.; Tuttle, T. R. *J. Phys. Chem. A* **1998**, *102*, 7787–7794.
- (35) Khramov, D. M.; Lynch, V. M.; Bielawski, C. W. *Organometallics* **2007**, *26*, 6042–6049.
- (36) Coe, B. J.; Glenwright, S. J. *Coord. Chem. Rev.* **2000**, *203*, 5–80.
- (37) Sashuk, V.; Peeck, L. H.; Plenio, H. *Chem.—Eur. J.* **2010**, *16*, 3983–3993.
- (38) Würtemberger, M.; Ott, T.; Döring, C.; Schaub, T.; Radius, U. *Eur. J. Inorg. Chem.* **2011**, *2011*, 405–415.
- (39) Cabeza, J. A.; del Río, I.; Miguel, D.; Sánchez-Vega, M. G. *Angew. Chem., Int. Ed.* **2008**, *47*, 1920–1922.
- (40) Concepcion, J. J.; Jurss, J. W.; Norris, M. R.; Chen, Z.; Templeton, J. L.; Meyer, T. J. *Inorg. Chem.* **2010**, *49*, 1277–1279.
- (41) Nyhlen, J.; Duan, L.; Åkermark, B.; Sun, L.; Privalov, T. *Angew. Chem., Int. Ed.* **2010**, *49*, 1773–1777.
- (42) Parent, A. R.; Crabtree, R. H.; Brudvig, G. W. *Chem. Soc. Rev.* **2013**, *42*, 2247–2252.